

# Compressibility and High-Pressure Structure of $\text{CaMg}_2\text{Bi}_2$ and $\text{YbMg}_2\text{Bi}_2$

Mario Calderón-Cueva,<sup>†,§</sup> Allison Pease,<sup>‡</sup> Cheng Peng,<sup>¶</sup> Wanyue Peng,<sup>†</sup> Megan Rylko,<sup>†</sup> Weiwei Xie,<sup>¶</sup> Susannah M. Dorfman,<sup>‡</sup> and Alexandra Zevalkink\*,<sup>†</sup>

<sup>†</sup>*Chemical Engineering and Materials Science Department, Michigan State University, East Lansing, MI 48824, USA*

<sup>‡</sup>*Department of Earth and Environmental Sciences, Michigan State University, East Lansing, MI 48824, USA*

<sup>¶</sup>*Chemistry Department, Michigan State University, East Lansing, MI 48824, USA*

<sup>§</sup>*Current Address: Mechanical and Aerospace Engineering, The George Washington University, Washington, D.C. 20052, USA*

E-mail: alexzev@msu.edu

## Abstract

Compounds with the formula  $AM_2X_2$  in the  $\text{CaAl}_2\text{Si}_2$  structure type have garnered increasing interest across various solid-state research domains, such as quantum topological and thermoelectric materials. Prior studies have identified high-pressure phase transitions in several compounds, including  $\text{Mg}_3\text{Sb}_2$ ,  $\text{Mg}_3\text{Bi}_2$ ,  $\text{CaMn}_2\text{Bi}_2$ , and  $\text{SrAl}_2\text{Si}_2$ . In this study, we investigate the structural behavior of  $\text{CaMg}_2\text{Bi}_2$  and  $\text{YbMg}_2\text{Bi}_2$  under varying pressure conditions. We synthesized crystals using the molten metal flux method and examined them through single-crystal synchrotron X-ray diffraction, employing diamond anvil cells to exert pressures up to 20 GPa. Our analysis reveals insights into the anisotropic compressibility of these materials, highlighting the more compressible and flexible octahedral  $A$ -Bi bonds as the primary contributors to this anisotropy. Moreover, we observed a phase transition in both  $\text{CaMg}_2\text{Bi}_2$  and  $\text{YbMg}_2\text{Bi}_2$  at pressures above 9.6 GPa and 8.7 GPa, respectively. The newly identified high-pressure phase exhibits a distortion of the original  $\text{CaAl}_2\text{Si}_2$  structure with space group  $C2/m$ . This high-pressure structure is distinct from that of related compounds (e.g.,  $\text{CaMn}_2\text{Bi}_2$ ,  $\text{MgMg}_2\text{Bi}_2$ ), the latter exhibiting a square pyramidal coordination for the  $M$  site.

## Introduction

In recent years, compounds in the  $AM_2X_2$  stoichiometry that crystallize in the  $\text{CaAl}_2\text{Si}_2$  structure type have been extensively studied for their thermoelectric performance,<sup>1-4</sup> quantum topological states,<sup>5,6</sup> and magnetic prop-

erties.<sup>7,8</sup> Compounds that form the  $\text{CaAl}_2\text{Si}_2$  structure type are highly tunable, as each  $A$ ,  $M$ , and  $X$  sites can accommodate a wide range of elements ( $A$  denotes rare-earth or alkaline-earth elements,  $M$  represents transition metals or group-13 elements, and  $X$  signifies group-14

or group-15 elements). The inherent tunability of this structure has inspired research efforts to explore the stability limits of this structure as well as the transport properties.<sup>9</sup>

For thermoelectric materials, low lattice thermal conductivity,  $\kappa_L$ , is a necessary characteristic. In the limit of phonon transport limited by Umklapp scattering,  $\kappa_L \propto v^2$ ,<sup>10</sup> where  $v$  is the velocity of collective lattice vibrations (*phonons*). It is often convenient to approximate the phonon velocity,  $v$ , as the low-frequency wave propagation speed, i.e. the *speed of sound*,  $v_s$ , which in turn, is related to the bond stiffness,  $k$ , and mass of the atoms,  $M$  by  $v_s \sim \sqrt{k/M}$ .<sup>11</sup> From these relations, it becomes evident that intrinsic low  $\kappa_L$  arises from soft bonds (low  $k$ ) and/or high mass  $M$ . A number of prior studies<sup>9,12-14</sup> have investigated bond stiffness in  $AMg_2Pn_2$  compounds via either acoustic measurements or via first principles lattice dynamics calculations, showing that the *A*-site cation plays an important role. Comparisons of compounds with  $A = \text{Mg}$  versus  $A = \text{Ca}$  or  $\text{Yb}$  have shown that the larger cations ( $\text{Ca}$  and  $\text{Yb}$ ) lead to higher experimental elastic constants and lower anharmonicity.<sup>15</sup> However, only a few studies<sup>16-18</sup> report their thermoelectric and topological properties, specifically for the  $\text{CaMg}_2\text{Bi}_2$  and  $\text{YbMg}_2\text{Bi}_2$  compounds. A less common approach to measuring bond stiffness is through the application of high pressure. By measuring the way in which the crystal structure evolves under applied pressure, one can simultaneously measure the compressibility of a solid and explore its stability limit with respect to high-pressure polymorphs.<sup>19,20</sup> High pressure also can be used to tune electronic and thermal properties of a material, making it a valuable tool for investigating transport phenomena<sup>21</sup>.

Although a large number of compounds form the  $\text{CaAl}_2\text{Si}_2$  structure (space group  $P\bar{3}m1$ ), there have only been a handful of high-pressure crystallographic investigations. These initial studies hint at a surprising diversity of high pressure structure transitions:  $\text{SrAl}_2\text{Si}_2$ <sup>22,23</sup> and  $\text{SrMn}_2\text{P}_2$ <sup>24</sup> transform into the well-known tetragonal ( $I4/mmm$ ) crystal structure, while  $\text{CaMn}_2\text{Bi}_2$ <sup>25</sup> and  $\text{MgMg}_2(\text{Sb,Bi})_2$ <sup>26</sup> were each

reported to transform into a different monoclinic structure (with space group  $P2_1/m$  and  $C2/m$ , respectively). The focus of the present work is on the two compounds,  $\text{CaMg}_2\text{Bi}_2$  and  $\text{YbMg}_2\text{Bi}_2$ . Using in-situ single crystal diffraction, we show that these compounds transform into a new monoclinic structure type, closely related to the one reported for  $\text{CaMn}_2\text{Bi}_2$ . Further, we track the evolution of the crystal structure as a function of pressure to extract volumetric, linear, and bond-specific compressibility of the  $\text{CaAl}_2\text{Si}_2$  structure. The present work aims to build on our prior work on  $\text{MgMg}_2\text{Bi}_2$ ,<sup>26</sup> by exploring how replacing  $\text{Mg}$  with larger  $\text{Ca}$  and  $\text{Yb}$  cations affects the stability of the ambient pressure phase and the details of the high pressure structure.

## Experimental Methods

### Polycrystalline Synthesis

For both the synthesis of single- and polycrystals, the following high-purity elements were used:  $\text{Ca}$  (dendritic pieces, 99.9%, Sigma-Aldrich),  $\text{Mg}$  (granules, Alfa Aesar 99.8%),  $\text{Sb}$  (shot, Alfa Aesar, 99.999%),  $\text{Bi}$  (shot, 99.99%, RotoMetal), and  $\text{Yb}$  (pieces, Sigma-Aldrich, 99.9%). Polycrystalline samples of  $\text{CaMg}_2\text{Bi}_2$  and  $\text{YbMg}_2\text{Bi}_2$  were synthesized by mixing stoichiometric amounts of their corresponding elements followed by spark plasma sintering (SPS). The elements were cut into small pieces and loaded into steel vials together with stainless-steel ball bearings inside an Argon-filled glovebox. The airtight vials were then placed into a SPEX mill and ball-milled for 60 minutes. After milling, the vials were returned to the glovebox and the fine powder was loaded into graphite dies for SPS using a Dr. Sinter SPS-211LX.

The sintering procedure for both compounds was the same, where the powders were subjected to a pressure of 31 MPa, heated to 700°C at a rate of 68 °C/min, and held at that temperature for 10 minutes. The target SPS temperature was selected to be 80% of the melting temperatures reported in Ref.,<sup>14</sup> while the pres-

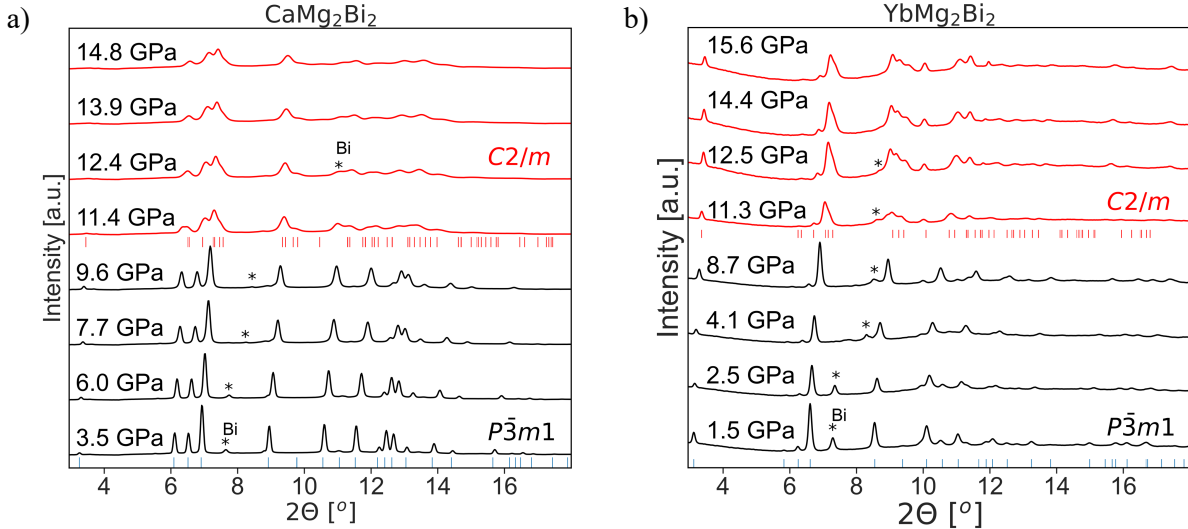


Figure 1: Powder XRD for a)  $\text{CaMg}_2\text{Bi}_2$  and b)  $\text{YbMg}_2\text{Bi}_2$  as a function of pressure shows evidence of phase transitions in the range of 9.6-11.4 GPa and 8.7-11.3 GPa, respectively. The trigonal phase ( $P\bar{3}m1$ ) is shown in black, and the high pressure monoclinic ( $C2/m$ ) phase is shown in red. Elemental Bi is present as an impurity in both samples, marked by asterisks.

sure and wait time were empirically determined to yield the desired phase. After that period, the pressure was immediately released and the samples were allowed to reach ambient temperature. The resulting consolidated disks were ground to fine powders and checked for phase purity using X-ray diffraction (XRD) with a Rigaku SmartLab Diffractometer with a  $\text{Cu K}\alpha$  source. The results of the Rietveld refinements, depicted in the SI Figure S3, revealed that the impurity content (elemental Bi) was less than 3% and 5% for  $\text{CaMg}_2\text{Bi}_2$  and  $\text{YbMg}_2\text{Bi}_2$ , respectively.

## Single-Crystal Synthesis

Single crystals of  $\text{CaMg}_2\text{Bi}_2$  and  $\text{YbMg}_2\text{Bi}_2$  were grown via the self-flux method, with a starting composition of  $\text{AMg}_4\text{Bi}_6$  ( $A=\text{Ca}, \text{Yb}$ ). The high quality of the crystals was confirmed by sharp diffraction spots in the precession images, as demonstrated in Figure S1 (Supplemental Information). After the ball-milling process, which was identical to the polycrystalline samples, the powders were then loaded into Canfield  $\text{Al}_2\text{O}_3$  crucibles and subsequently sealed in quartz ampules under vacuum ( $< 10^{-4}$  Torr). The quartz ampules were then placed in a box furnace, where the furnace temperature

was brought to  $900^\circ\text{C}$  in 8 hr, then to  $850^\circ\text{C}$  in 1 hr, and cooled to  $650^\circ\text{C}$  in 40 hours. After soaking for 48 hours at  $650^\circ\text{C}$ , the ampules were centrifuged to remove the liquid flux from the desired crystallized samples. As a result, large crystals (approx. 5 mm in their longest dimension) were obtained. These crystals were then easily cleaved into smaller pieces with surgical blades, which yielded smaller pieces with plate-like geometry. The pieces that exhibited faceted morphology, and approx.  $50\ \mu\text{m}$  in their longest dimension, were selected and screened for crystallinity and phase purity using a Rigaku XtaLAB Synergy S Diffractometer.

## High-pressure X-ray diffraction

High-pressure diffraction experiments were conducted at the Advanced Photon Source (APS) in Argonne National Lab, using diamond anvil cells (DACs) to apply hydrostatic pressure environments to the samples. X-ray diffraction patterns were collected during the compression cycle.

For powder diffraction of  $\text{YbMg}_2\text{Bi}_2$ , pairs of flat,  $800\text{-}\mu\text{m}$ -culet diamond anvils (BX90<sup>27</sup> design) were used. A precompressed powder of the desired composition was loaded into a  $410\text{-}\mu\text{m}$  hole within a pre-indented steel gasket.

A methanol-ethanol (4:1) mixture served as a pressure transmitting medium, and a 10- $\mu\text{m}$  ruby crystal was used as the pressure indicator. The diffraction patterns were collected at beamline 13-BM-C, using X-rays with a wavelength  $\lambda = 0.413 \text{ \AA}$ .  $\text{CaMg}_2\text{Bi}_2$  powder diffraction experiments were carried out at APS beamline 16 BM-D, with X-ray light of  $\lambda = 0.434 \text{ \AA}$ , using flat, 300- $\mu\text{m}$ -culet diamond anvils (BX90 design), and Neon as the pressure transmitting medium, using the COMPRES-GSECARS gas loading system.<sup>28</sup> A pre-indented rhenium gasket was used, in which a hole of  $\sim 150 \mu\text{m}$  in diameter was drilled.

For single crystal experiments, diamond anvil pairs of flat 300- $\mu\text{m}$  culets (custom CVD, conical Boehler-Almax design, with (Vascomax<sup>®</sup>) stainless steel were used, with an effective aperture of  $80^\circ$ . Pre-screened single crystals of the desired compositions were loaded into a 150- $\mu\text{m}$  hole within a pre-indented Re gasket. Ne gas or a methanol-ethanol (4:1) mixture was used as the pressure transmitting medium, and a 10- $\mu\text{m}$  ruby crystal was used as the pressure indicator. Ne gas was loaded at GSECARS (Sector 13)<sup>28</sup> at APS. Single-crystal X-ray diffraction (SC-XRD) experiments were carried out in beamline 13-BM-C, with X-ray wavelength source of  $\lambda = 0.434 \text{ \AA}$ . The inset images in Figure 2a-b) show the loading conditions of the  $\text{CaMg}_2\text{Bi}_2$  and  $\text{YbMg}_2\text{Bi}_2$  crystals inside the DACs after gas-loading. The diffraction patterns were collected with a Dectris Pilatus3 1M Pixel Array Detector.

The diffraction data for single-crystalline  $\text{CaMg}_2\text{Bi}_2$  and  $\text{YbMg}_2\text{Bi}_2$  was collected by APEX3,<sup>29</sup> integrated using SAINT<sup>30</sup> code and corrected for absorption with the SADABS method.<sup>31</sup> The structure was solved by the SHELXS routine.<sup>32</sup> For both compositions, the structures were refined in the OLEX2 Suite,<sup>33</sup> by the full-matrix least-square methods of SHELXL. All refined structural data was obtained from the single crystal samples. The powder samples were used only for initial determination of the phase transition pressure, and Rietveld fits to the high-pressure phases (see SI Figure S4) were used as an additional verification of the structural model obtained from

single crystal refinements. Rietveld refinements were performed in GSAS-II.<sup>34</sup>

After the crystallographic refinements, the parameters of the equations of state (EoS) for the two compounds were fit to data via the least-squares fitting routine of the EoSFit7 software.<sup>35</sup> The volume compressibilities were fit using a second-order Birch-Murnaghan (BM) EoS.<sup>36,37</sup> Polyhedral volumes and uncertainties were calculated from bond lengths using the approach described in the Supplemental Information section S2.

## Results and Discussion

The powder and single crystals of  $\text{CaMg}_2\text{Bi}_2$  and  $\text{YbMg}_2\text{Bi}_2$  form the trigonal  $\text{CaAl}_2\text{Si}_2$  structure (space group  $P\bar{3}m1$ , as shown in Figure 4b), as reported in prior literature<sup>38,39</sup>. The powder XRD patterns on polycrystalline samples were initially collected for  $\text{CaMg}_2\text{Bi}_2$  and  $\text{YbMg}_2\text{Bi}_2$  as a function of pressure up to 18 GPa and 17.5 GPa, respectively. Figure 1 shows the patterns at selected pressures. In both samples, the trigonal phase is shown in black. New peaks begin to appear in the diffraction patterns of  $\text{CaMg}_2\text{Bi}_2$  and  $\text{YbMg}_2\text{Bi}_2$  above 9.6 and 8.7 GPa, respectively, indicating the beginning of a phase transition.

Rietveld analysis of the powder diffraction data above 11.3 GPa was initially attempted using two known high-pressure structures of similar compounds, namely that of  $C2/m$ - $\text{Mg}_3\text{Sb}_2$ <sup>26</sup> and  $P2_1/m$ - $\text{CaMn}_2\text{Bi}_2$ .<sup>25</sup> However, these solutions did not provide an acceptable fit. For that reason, single-crystal XRD experiments were conducted for both compositions, ultimately showing that  $\text{CaMg}_2\text{Bi}_2$  and  $\text{YbMg}_2\text{Bi}_2$  crystallize in a new structure type with space group  $C2/m$ . In the following sections, we present first an analysis of the compressibility of each compound within the stability range of the trigonal phase, followed by a description of the high-pressure structures of both compounds, based on the single-crystal data. Tables S1-S3 in the Supplemental Information summarize the relevant experimental data for the Birch-Murnaghan fits to single-crystal data obtained

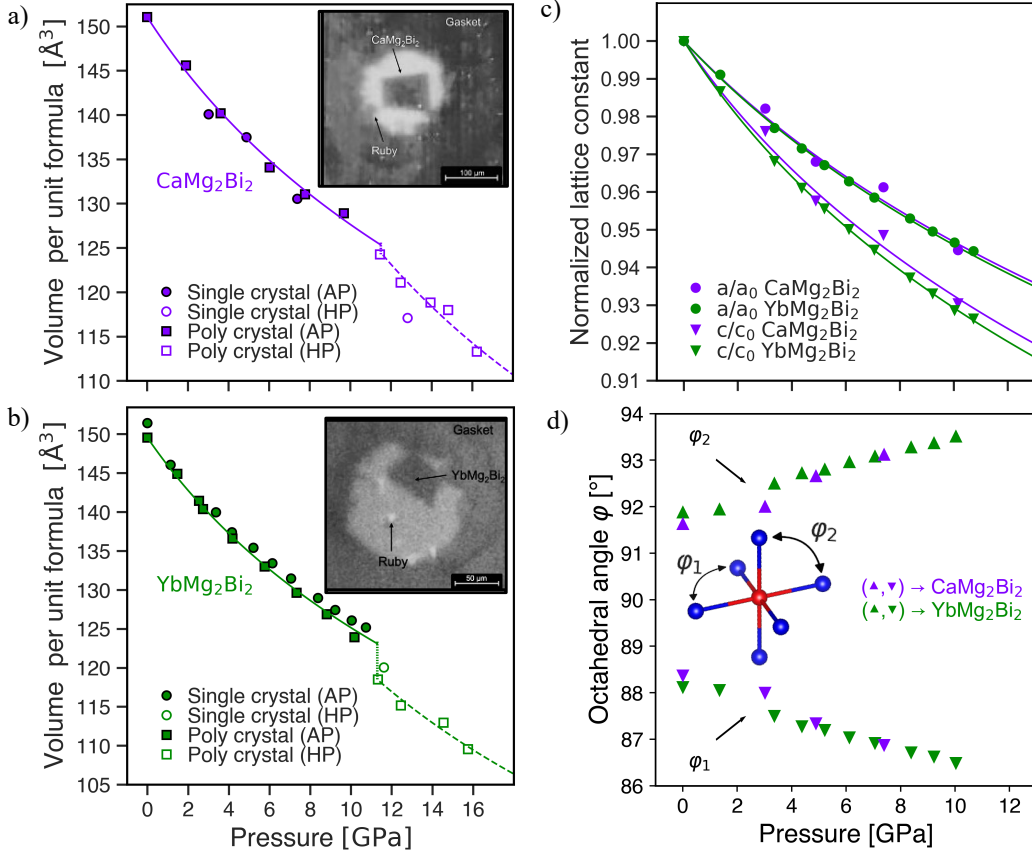


Figure 2: Experimental single-crystal (circles) and polycrystalline (squares) unit cell volumes as a function of pressure for a) CaMg<sub>2</sub>Bi<sub>2</sub> and b) YbMg<sub>2</sub>Bi<sub>2</sub> and their corresponding images inside DACs after pressure-medium-loading (see insets, methanol-ethanol for CaMg<sub>2</sub>Bi<sub>2</sub> and Ne for YbMg<sub>2</sub>Bi<sub>2</sub>). The open symbols in a) and b) show the volume/formula unit of the high-pressure phase. c) The normalized lattice parameters d) and octahedral angles vs. pressure for CaMg<sub>2</sub>Bi<sub>2</sub> (magenta) and YbMg<sub>2</sub>Bi<sub>2</sub> (green) from SC-XRD. Dashed lines represent 2<sup>nd</sup> order BM fits.

for both compounds. These tables show selected pressure steps for both the ambient- and high-pressure phases.

## Compressibility of CaMg<sub>2</sub>Bi<sub>2</sub> and YbMg<sub>2</sub>Bi<sub>2</sub>

*Volume compressibility:* The experimental unit cell volume as a function of pressure is shown in Figure 2a-b) for CaMg<sub>2</sub>Bi<sub>2</sub> and YbMg<sub>2</sub>Bi<sub>2</sub>. Filled symbols correspond to the ambient-pressure trigonal structure type and open symbols to the high-pressure structure type, which will be discussed further in the next section. The volumetric bulk modulus for the trigonal ambient-pressure ( $B_0$ ) phases were calculated by fitting the pressure-volume data (using both single and polycrystalline data points) to the

second-order Birch-Murnaghan (BM) equation of state:<sup>36,37,40</sup>

$$P(V) = \frac{3B_0}{2} \left[ \left( \frac{V_0}{V} \right)^{\frac{7}{3}} - \left( \frac{V_0}{V} \right)^{\frac{5}{3}} \right] \quad (1)$$

where  $P$  is the applied pressure (determined from the ruby standard),  $V$  the observed unit cell volume, and  $V_0$  the reference unit cell volume. Note that  $B_0$  corresponds to the bulk modulus at ambient pressure, and is treated here as a pressure-independent fitting parameter. The BM fits to the volume data are shown as the purple and green curves in Figure 2, and the resulting  $B_0$  values are listed in Table 1.

CaMg<sub>2</sub>Bi<sub>2</sub> and YbMg<sub>2</sub>Bi<sub>2</sub> were found to have nearly identical zero-pressure  $B_0$  ( $\sim 37$ -38 GPa). This is not surprising, given the sim-

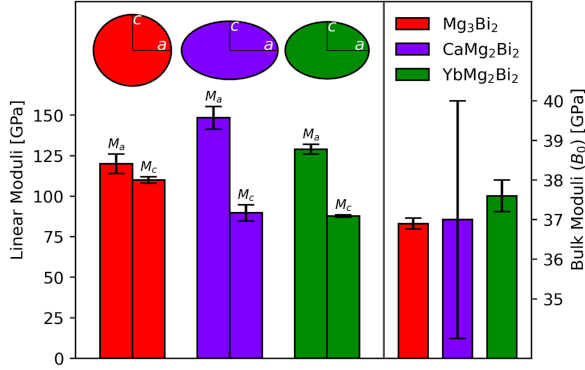


Figure 3: Linear (left) and bulk (right) moduli comparison for  $AMg_2Bi_2$  ( $A = Ca, Mg, Yb$ ) at ambient pressure with their corresponding uncertainties.  $MgMg_2Bi_2$  data taken from Ref. <sup>26</sup>

ilar ionic radii of  $Yb^{2+}$  ( $1.02 \text{ \AA}^{41}$ ) and  $Ca^{2+}$  ( $1.00 \text{ \AA}^{41}$ ), and similar ambient pressure volume. Our results are also in agreement with previously reported values obtained using ultrasonic measurements on bulk polycrystalline samples (36 GPa and 38 GPa for  $CaMg_2Bi_2$  and  $YbMg_2Bi_2$ , respectively<sup>15</sup>).

At the phase transition from the trigonal to monoclinic cell, a small decrease in the volume per formula unit of  $\sim 0.9\%$  and  $\sim 3.7\%$  for  $CaMg_2Bi_2$  and  $YbMg_2Bi_2$ , respectively, can be observed. Above the phase transition, we have insufficient data points to reliably determine the elastic moduli of the high-pressure structure type (the lattice parameters vs. pressure for the  $C2/m$  are shown in the Fig. S2). However, BM fits are shown as dashed curves to provide a "guide to the eye", and these were to estimate the change in volume at the phase transition pressure.

*Linear compressibility:* Returning to the trigonal structure type, Figure 2c) shows the normalized lattice parameters,  $a/a_0$  and  $c/c_0$ , as a function of pressure, obtained from single crystal data. From these, the linear bulk moduli ( $M_a$  and  $M_c$ ) were extracted using a linearized 2<sup>nd</sup> order BM equation, given by:

$$P(l) = \frac{3M_l}{2} \left[ \left( \frac{l_0^3}{l^3} \right)^{\frac{7}{3}} - \left( \frac{l_0^3}{l^3} \right)^{\frac{5}{3}} \right]. \quad (2)$$

Here,  $l$  represents either the lattice parameter  $a$  or  $c$ ,<sup>42</sup>. The values at ambient pressure,  $a_0$  and  $c_0$ , were treated as fitting parameters. Figure 2c) clearly shows that  $c$  is more compressible than  $a$  for both compounds. Accordingly, the linear moduli obtained from the BM fits along  $c$  are much smaller ( $M_c \sim 90$  GPa) than those obtained along  $a$  ( $M_a \sim 130$ - $140$  GPa). Figure 3 shows a comparison of the bulk and linear elastic moduli of  $MgMg_2Bi_2$ ,  $CaMg_2Bi_2$ , and  $YbMg_2Bi_2$ . The ellipses illustrate how the linear modulus varies as a function of crystallographic direction in the  $a$ - $c$  plane. Conceptually, they can be understood as the final cross sections of spherical particles subjected to isotropic pressure. We can see that even though the bulk moduli are nearly identical regardless of cation species, the degree of anisotropy varies strongly. Compared with  $MgMg_2Bi_2$ , the larger cations in the present compounds lead to decreased stiffness (smaller  $M_c$ ) along the  $c$ -axis, and increased stiffness along the  $a$ - and  $b$ -axes (larger  $M_a$ ). This would be expected to lead, in turn, to anisotropy in the thermal transport in single crystals.

*Compressibility of polyhedra and individual bonds:* To better understand the underlying factors controlling the anisotropic compressibility, we consider how individual bond lengths and bond angles evolve as a function of pressure.<sup>43</sup> As shown in Fig. 4b), the trigonal  $AMg_2Bi_2$  ( $A = Ca, Bi$ ) structure consists of layers of  $[Mg_2Bi_2]^{2-}$ , in which the Mg atom (cyan) is tetrahedrally-coordinated by Bi (blue). Each tetrahedron shares three edges with neighboring tetrahedra. The tetrahedral layers are separated by the divalent cations (red), i.e., trigonal layers of cations ( $Ca^{2+}$  or  $Yb^{2+}$ ) that are octahedrally coordinated by six Bi atoms. The regular octahedra possess one unique bond ( $d1$ ) only. In contrast, the tetrahedra have two distinct bonds, one apical bond ( $d2$ ) and three basal bonds ( $d3$ ). Accurate Mg positions, which are needed to obtain  $d2$  and  $d3$  as a function of pressure, could only be refined from the  $YbMg_2Bi_2$  SC-XRD data, but not for  $CaMg_2Bi_2$ . Therefore, the pressure-dependent bond lengths are only shown for  $YbMg_2Bi_2$  (Figure 4d). However, the overall volume of

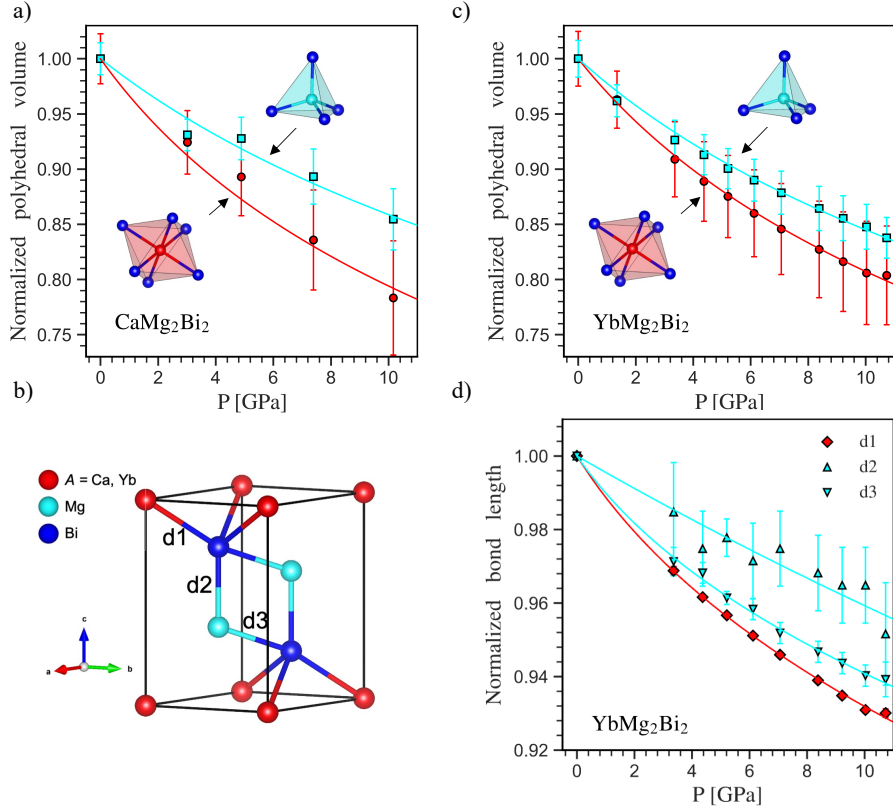


Figure 4: Normalized polyhedral volume vs. pressure below the phase transition for a)  $\text{CaMg}_2\text{Bi}_2$  and c)  $\text{YbMg}_2\text{Bi}_2$  from SC-XRD. b) The ambient pressure trigonal structure of  $\text{AMg}_2\text{Bi}_2$  ( $A = \text{Ca}, \text{Yb}$ ), space group  $P\bar{3}m1$ , showing the octahedral ( $d1$ ) and tetrahedral bonds ( $d2$  and  $d3$ ) d) Normalized bond length vs. pressure for  $\text{YbMg}_2\text{Bi}_2$  from SC-XRD highlights more compressible octahedral bond.

Table 1: Summary of the fitted ambient-pressure moduli for the trigonal  $\text{CaMg}_2\text{Bi}_2$  and  $\text{YbMg}_2\text{Bi}_2$  compounds. Bulk modulus ( $B_0$ ), linear moduli in  $a$ - and  $c$ -directions ( $M$ ), and polyhedral moduli ( $K_{tet}$ ,  $K_{oct}$ ), and bond-specific moduli ( $K_{d1}$ ,  $K_{d2}$ ,  $K_{d3}$ ) are included.

	$\text{CaMg}_2\text{Bi}_2$	$\text{YbMg}_2\text{Bi}_2$
Zero-pressure moduli (GPa)		
Bulk modulus (AP), $B_0$	$37 \pm 3$	$37.6 \pm 0.4$
Linear modulus along $a$ , $M_a$	$148.4 \pm 7$	$129.0 \pm 3$
Linear modulus along $c$ , $M_c$	$89.7 \pm 5$	$87.8 \pm 0.8$
Tetrahedron modulus, $K_{tet}$	$48 \pm 1$	$42.4 \pm 0.25$
Octahedron modulus, $K_{oct}$	$27.3 \pm 0.15$	$30.4 \pm 0.1$
Modulus of bond $d1$ , $K_{d1}$	–	$96 \pm 1.5$
Modulus of bond $d2$ , $K_{d2}$	–	$168 \pm 15$
Modulus of bond $d3$ , $K_{d3}$	–	$119 \pm 2.5$

each polyhedral environment (octahedral and tetrahedral) as well as the Bi- $A$ -Bi bond angles could be obtained using only the refined Bi position, and was therefore calculated for both

compounds.

The polyhedral volumes as a function of pressure are shown in Fig. 4a) & c). The uncertainty was estimated using an error propa-

gation method discussed in detail in the Supporting Information Section S2. The experimental data clearly demonstrate that, for both compounds, the octahedral environment compresses at a faster rate than the tetrahedral environment. This can be quantified using a modified version of Eq. 1, in which the unit cell volume is replaced by the polyhedral volume, yielding zero-pressure “polyhedra bulk moduli” (defined here as  $K_{oct}$  and  $K_{tet}$ , listed in Table 1).<sup>44</sup> The BM fits are shown as dashed curves in Fig. 4a) & c). For both  $\text{CaMg}_2\text{Bi}_2$  and  $\text{YbMg}_2\text{Bi}_2$ , the tetrahedron bulk modulus,  $K_{tet}$ , is considerably larger than the octahedron bulk  $K_{oct}$ . As a result, in both compounds, the overall bulk modulus lies between that of the tetrahedral modulus and the octahedral modulus.

Diving deeper, we find that the octahedral environment is more compressible than the tetrahedral one for two reasons; first, the octahedral bonds are more compliant, and second, the octahedral angles vary with pressure, allowing for further volume compression. The former can be seen in Figure 4d), which shows  $d1$ ,  $d2$ , and  $d3$  as a function of pressure in  $\text{YbMg}_2\text{Bi}_2$ . Note that uncertainty in the positions of the light Mg atoms leads to large uncertainty in  $d2$  and  $d3$ . Initial values of bond lengths for  $\text{YbMg}_2\text{Bi}_2$  are  $d1 = 3.2838(3) \text{ \AA}$ ,  $d2 = 2.8990(3) \text{ \AA}$ ,  $d3 = 2.9689(2) \text{ \AA}$ ; Figure 4d) clearly shows a faster compression with pressure of the octahedral bond  $d1$  with respect to the other bonds. The individual bond moduli ( $K_{di}$ , where  $i = 1, 2, \text{ or } 3$ ) were obtained using a modified version of Eq. 2, and are reported in Table 1. The 2<sup>nd</sup>-order BM fits are shown as dashed lines in Fig. 4d). The octahedral bond angles,  $\phi_1$  and  $\phi_2$ , are also allowed to vary in the trigonal symmetry. Figure 2d) shows the evolution of these two angles as a function of pressure in  $\text{CaMg}_2\text{Bi}_2$  and  $\text{YbMg}_2\text{Bi}_2$ . In an ideal octahedron, these angles would be  $90^\circ$ . At ambient pressure, the angles are  $88^\circ$  and  $92^\circ$  (they are nearly identical regardless of cation species). As pressure increases, these angles deviate further from  $90^\circ$ , indicating a distortion of the ideal octahedral geometry, allowing the structure to further compress in the  $c$ -direction. This flexibility, together with the more compliant octahe-

dral bonds, explain why the  $c$ -axis is more compressible (softer) than the  $a$ -axis in this structure type.

## High-Pressure Crystal Structure

As previously mentioned, a high-pressure structural transformation for both compounds was first observed in the powder samples at pressures between 9.5-11.4 GPa and 8.7-11.3 GPa in  $\text{CaMg}_2\text{Bi}_2$  and  $\text{YbMg}_2\text{Bi}_2$ , respectively. The powder data, which is more likely than single-crystal data to exhibit two-phase equilibrium, displays peak broadening that is too severe to allow for the refinement of relative phase fractions. This is relevant to  $\text{CaMg}_2\text{Bi}_2$ , where at 11.3 GPa, the ambient and high-pressure phases may co-exist. The single crystal data confirmed these phase transition pressures. The high-pressure structures were refined as having the monoclinic crystal system with a unit cell corresponding to twice that of the  $P\bar{3}m1$  unit cell. The final refined space group resulting in a solution with physical interatomic distances was  $C2/m$ . The position determination of Mg atoms for both compounds proved to be challenging due to its low mass compared to the other atoms. Several possible solutions were explored, and ultimately, the only physical solution put the Mg atoms in a coordination environment very similar to that of the ambient-pressure structure. This new structure can be described as a slightly distorted variant of the  $P\bar{3}m1$  structure, in which the coordination environments are the same (i.e., alternating  $A$ -centered octahedral layers and Mg-centered tetrahedral layers are maintained), but the unit cell is distorted with a  $\beta = 92^\circ$  and  $\beta = 94^\circ$  for  $\text{CaMg}_2\text{Bi}_2$  and  $\text{YbMg}_2\text{Bi}_2$ , respectively. The crystallographic information is summarized in Table S3.

As shown in Fig. 5b-c), other  $AM_2X_2$  compounds at high pressure, namely  $\text{MgMg}_2Pn_2$  ( $Pn = \text{Sb, Bi}$ ) and  $\text{CaMn}_2\text{Bi}_2$ , also experience displacive phase transformations to monoclinic symmetry, but with more dramatic changes to the coordination environments than in the present compounds. In the case of  $\text{MgMg}_2\text{Bi}_2$  and  $\text{MgMg}_2\text{Sb}_2$ , a monoclinic symmetry ( $Z = 4$ ,

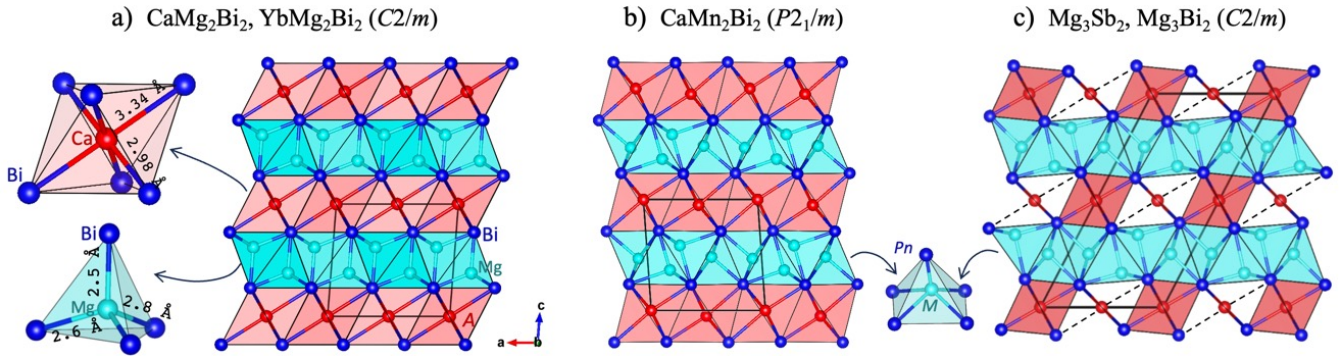


Figure 5: a) High-pressure ( $C2/m$ ) structures for  $\text{CaMg}_2\text{Bi}_2$  and  $\text{YbMg}_2\text{Bi}_2$  with detailed octahedron (top left) and detailed tetrahedron (bottom left). Bond lengths are given for  $\text{CaMg}_2\text{Bi}_2$  at 12.82 GPa. In the high-pressure structures of b)  $\text{CaMn}_2\text{Bi}_2$  space group  $P2_1/m$  and c)  $\text{MgMg}_2Pn_2$  ( $Pn = \text{Sb, Bi}$ ), space group  $C2/m$ , the ambient-pressure tetrahedral environment becomes square pyramidal.<sup>25,26</sup>

$C2/m$ ) was reported above 7.8 and 4.0 GPa, respectively.<sup>26</sup> This trigonal-to-monoclinic transformation is accompanied by octahedral bond-breaking at every other cation site, as depicted in Fig. 5c) by the dashed lines. In  $\text{CaMn}_2\text{Bi}_2$ , the monoclinic phase forming above 2 GPa ( $Z = 2$ ,  $P2_1/m$ ),<sup>25</sup> shows instead only a slight elongation of the octahedral bonds. However, in both of these alternative high-pressure structures (and in contrast to the subject of this study), the tetrahedral environment in the  $M_2X_2$  layer is transformed into a square pyramidal one (shown by the cyan polyhedra).

## Conclusion

The higher compressibility of  $\text{CaMg}_2\text{Bi}_2$  and  $\text{YbMg}_2\text{Bi}_2$  in the  $c$ -direction arises from the soft tetrahedral bonds, while the  $a$ -direction compressibility is smaller due to stiffer octahedral bonds. The  $AM_2X_2$  compounds studied here have 3D, edge-sharing octahedra as well as tetrahedra. For this reason, to understand the bulk modulus, it is necessary to study it as a combined effect of different bond strengths and edge-sharing 3D polyhedra. Additionally, a high-pressure structure (monoclinic,  $C2/m$ ) was discovered above 9.6 GPa and 8.7 GPa for  $\text{CaMg}_2\text{Bi}_2$  and  $\text{YbMg}_2\text{Bi}_2$ , respectively. This displacive phase transition is characterized by a change in the Mg-Bi coordination environment from tetrahedral to square pyramidal coordina-

tion. The study of the elastic properties and phase stability of these compounds serves as a basis for understanding the interplay between the bonding nature and thermal transport of this class of thermoelectric materials.

## Acknowledgements

The research was supported by the U.S. Department of Energy, Office of Basic Energy Sciences, Division of Materials Sciences and Engineering under Award DE-SC0019252. Use of the COMPRES-GSECARS gas loading system was supported by COMPRES under NSF Cooperative Agreement EAR-1661511 and by GSECARS through NSF grant EAR-1634415. This research used resources of the Advanced Photon Source, a U.S. Department of Energy (DOE) Office of Science User Facility operated for the DOE Office of Science by Argonne National Laboratory under Contract No. DE-AC02-06CH11357.

The authors gratefully acknowledge Dongzhou Zhang and Jingui Xu for their help with high-pressure X-ray diffraction experiments, Sergey N. Tkachev for his help with gas loading of diamond anvil cells at APS, and Richard Staples for his support at the Center for Crystallography at Michigan State University.

## References

- (1) Gascoin, F.; Ottensmann, S.; Stark, D.; Haïle, S. M.; Snyder, G. J. Zintl phases as thermoelectric materials: tuned transport properties of the compounds  $\text{Ca}_x\text{Yb}_{1-x}\text{Zn}_2\text{Sb}_x$ . *Advanced Functional Materials* **2005**, *15*, 1860–1864.
- (2) Wang, X.-J.; Tang, M.-B.; Chen, H.-H.; Yang, X.-X.; Zhao, J.-T.; Burkhardt, U.; Grin, Y. Synthesis and high thermoelectric efficiency of Zintl phase  $\text{YbCd}_{2-x}\text{Zn}_x\text{Sb}_2$ . *Appl. Phys. Lett.* **2009**, *94*, 092106.
- (3) Wood, M.; Aydemir, U.; Ohno, S.; Snyder, G. J. Observation of valence band crossing: the thermoelectric properties of  $\text{CaZn}_2\text{Sb}_2$ - $\text{CaMg}_2\text{Sb}_2$  solid solution. *Journal of Materials Chemistry A* **2018**, *6*, 9437–9444.
- (4) Shuai, J.; Geng, H.; Lan, Y.; Zhu, Z.; Wang, C.; Liu, Z.; Bao, J.; Chu, C.-W.; Sui, J.; Ren, Z. Higher thermoelectric performance of Zintl phases  $(\text{Eu}_{0.5}\text{Yb}_{0.5})_{1-x}\text{Ca}_x\text{Mg}_2\text{Bi}_2$  by band engineering and strain fluctuation. *Proceedings of the National Academy of Sciences* **2016**, *113*, E4125–E4132.
- (5) Chang, T.-R.; Pletikovic, I.; Kong, T.; Bian, G.; Huang, A.; Denlinger, J.; Kushwaha, S. K.; Sinkovic, B.; Jeng, H.-T.; Valla, T.; others Realization of a type-II nodal-line semimetal in  $\text{Mg}_3\text{Bi}_2$ . *Advanced Science* **2019**, *6*, 1800897.
- (6) Feng, L.-Y.; Villaos, R. A. B.; Maghirang, A. B.; Huang, Z.-Q.; Hsu, C.-H.; Lin, H.; Chuang, F.-C. Prediction of topological Dirac semimetal in Ca-based Zintl layered compounds  $\text{CaM}_2\text{X}_2$  (M= Zn or Cd; X= N, P, As, Sb, or Bi). *Scientific reports* **2022**, *12*, 1–8.
- (7) Sangeetha, N.; Pandey, A.; Benson, Z. A.; Johnston, D. Strong magnetic correlations to 900 K in single crystals of the trigonal antiferromagnetic insulators  $\text{SrMn}_2\text{As}_2$  and  $\text{CaMn}_2\text{As}_2$ . *Physical Review B* **2016**, *94*, 094417.
- (8) Berry, T.; Stewart, V. J.; Redemann, B. W.; Lygouras, C.; Varnava, N.; Vanderbilt, D.; McQueen, T. M. A-type antiferromagnetic order in the Zintl-phase insulator  $\text{EuZn}_2\text{P}_2$ . *Physical Review B* **2022**, *106*, 054420.
- (9) Peng, W.; Chanakian, S.; Zevalkink, A. Crystal chemistry and thermoelectric transport of  $\text{AM}_2\text{X}_2$  compounds. *Inorganic Chemistry Frontiers* **2018**, *5*, 1744–1759.
- (10) Toberer, E. S.; May, A. F.; Snyder, G. J. Zintl chemistry for designing high efficiency thermoelectric materials. *Chemistry of Materials* **2010**, *22*, 624–634.
- (11) Zeier, W. G.; Zevalkink, A.; Gibbs, Z. M.; Hautier, G.; Kanatzidis, M. G.; Snyder, G. J. Thinking like a chemist: intuition in thermoelectric materials. *Angewandte Chemie International Edition* **2016**, *55*, 6826–6841.
- (12) Ding, J.; Lanigan-Atkins, T.; Calderon-Cueva, M.; Banerjee, A.; Abernathy, D. L.; Said, A.; Zevalkink, A.; Delaire, O. Soft anharmonic phonons and ultralow thermal conductivity in  $\text{Mg}_3(\text{Sb,Bi})_2$  thermoelectrics. *Submitted* **2020**,
- (13) Singh, D. J.; Parker, D. Electronic and transport properties of Zintl phase  $\text{AeMg}_3\text{Pn}_2$ ,  $\text{Ae} = \text{Ca, Sr, Ba}$ ,  $\text{Pn} = \text{As, Sb, Bi}$  in relation to  $\text{Mg}_3\text{Sb}_2$ . *J. Appl. Phys.* **2013**, *114*, 143703, First principles calculations of the electronic structure and transport properties of some 122 compounds including  $\text{Mg}_3\text{Sb}_2$ . This is the only paper that have discussed phonon DOS of these compounds at that time, even though not much insight about phonon properties.

- (14) May, A. F.; McGuire, M. A.; Singh, D. J.; Ma, J.; Delaire, O.; Huq, A.; Cai, W.; Wang, H. Thermoelectric transport properties of  $\text{CaMg}_2\text{Bi}_2$ ,  $\text{EuMg}_2\text{Bi}_2$ , and  $\text{YbMg}_2\text{Bi}_2$ . *Physical Review B* **2012**, *85*, 035202.
- (15) Peng, W.; Petretto, G.; Rignanesi, G.-M.; Hautier, G.; Zevalkink, A. An unlikely route to low lattice thermal conductivity: Small atoms in a simple layered structure. *Joule* **2018**, *2*, 1879–1893.
- (16) Kundu, A. K.; Roy, T.; Pakhira, S.; Wu, Z.-B.; Tsujikawa, M.; Shirai, M.; Johnston, D.; Pasupathy, A. N.; Valla, T. Topological electronic structure of  $\text{YbMg}_2\text{Bi}_2$  and  $\text{CaMg}_2\text{Bi}_2$ . *npj Quantum Materials* **2022**, *7*, 67.
- (17) Sun, J.; Shuai, J.; Ren, Z.; Singh, D. J. Computational modelling of the thermoelectric properties of p-type Zintl compound  $\text{CaMg}_2\text{Bi}_2$ . *Materials Today Physics* **2017**, *2*, 40–45.
- (18) Sun, J.; Singh, D. J. Thermoelectric properties of  $\text{AMg}_2\text{X}_2$ ,  $\text{AZn}_2\text{Sb}_2$  ( $\text{A} = \text{Ca}, \text{Sr}, \text{Ba}$ ;  $\text{X} = \text{Sb}, \text{Bi}$ ), and  $\text{Ba}_2\text{ZnX}_2$  ( $\text{X} = \text{Sb}, \text{Bi}$ ) Zintl compounds. *Journal of Materials Chemistry A* **2017**, *5*, 8499–8509.
- (19) Walsh, J. P.; Freedman, D. E. High-pressure synthesis: a new frontier in the search for next-generation intermetallic compounds. *Accounts of chemical research* **2018**, *51*, 1315–1323.
- (20) Badding, J. V. High-pressure synthesis, characterization, and tuning of solid state materials. *Annu. Rev. Mater. Sci.* **1998**, *28*, 631–658.
- (21) Zhang, H.; Zhang, C.; Gregory, D. H.; Yin, Z.; Wang, Y.; He, P.; Guo, X. A review of pressure manipulating structure and performance in thermoelectrics. *Journal of Physics D: Applied Physics* **2023**,
- (22) Zevalkink, A.; Bobnar, M.; Schwarz, U.; Grin, Y. Making and Breaking Bonds in Superconducting  $\text{SrAl}_{4-x}\text{Si}_x$  ( $0 \leq x \leq 2$ ). *Chem. Mater.* **2017**, *29*, 1236–1244.
- (23) Strikos, S.; Joseph, B.; Alabarse, F. G.; Valadares, G.; Costa, D. G.; Capaz, R. B.; El-Massalami, M. Pressure dependence of room-temperature structural properties of  $\text{CaAl}_2\text{Si}_2$ . *Journal of Physics: Condensed Matter* **2020**, *32*, 365403.
- (24) Xie, W.; Winiarski, M. J.; Klimczuk, T.; Cava, R. J. A tetragonal polymorph of  $\text{SrMn}_2\text{P}_2$  made under high pressure—theory and experiment in harmony. *Dalton Trans.* **2017**, *46*, 6835–6838.
- (25) Gui, X.; Finkelstein, G. J.; Chen, K.; Yong, T.; Dera, P.; Cheng, J.; Xie, W. Pressure-Induced Large Volume Collapse, Plane-to-Chain, Insulator to Metal Transition in  $\text{CaMn}_2\text{Bi}_2$ . *Inorg. Chem.* **2019**, *58*, 8933–8937.
- (26) Calderón-Cueva, M.; Peng, W.; Clarke, S. M.; Ding, J.; Brugman, B. L.; Levental, G.; Balodhi, A.; Rylko, M.; Delaire, O.; Walsh, J. P.; others Anisotropic structural collapse of  $\text{Mg}_3\text{Sb}_2$  and  $\text{Mg}_3\text{Bi}_2$  at high pressure. *Chemistry of Materials* **2021**, *33*, 567–573.
- (27) Kantor, I.; Prakapenka, V.; Kantor, A.; Dera, P.; Kurnosov, A.; Sinogeikin, S.; Dubrovinskaya, N.; Dubrovinsky, L. BX90: A new diamond anvil cell design for X-ray diffraction and optical measurements. *Review of Scientific Instruments* **2012**, *83*.
- (28) Rivers, M.; Prakapenka, V. B.; Kubo, A.; Pullins, C.; Holl, C. M.; Jacobsen, S. D. The COMPRES/GSECARS gas-loading system for diamond anvil cells at the Advanced Photon Source. *High Pressure Research* **2008**, *28*, 273–292.

- (29) Bruker, M. APEX3 and SADABS. *Bruker AXS Inc., Wisconsin, USA* **2016**,
- (30) Bruker, A. SAINT and SADABS. *Bruker AXS Inc., Madison, Wisconsin, USA* **2009**,
- (31) Krause, L.; Herbst-Irmer, R.; Sheldrick, G. M.; Stalke, D. Comparison of silver and molybdenum microfocus X-ray sources for single-crystal structure determination. *Journal of applied crystallography* **2015**, *48*, 3–10.
- (32) Sheldrick, G. M. A short history of SHELX. *Acta Crystallographica Section A: Foundations of Crystallography* **2008**, *64*, 112–122.
- (33) Dolomanov, O. V.; Blake, A. J.; Champness, N. R.; Schröder, M. OLEX: new software for visualization and analysis of extended crystal structures. *J. Appl. Crystallogr.* **2003**, *36*, 1283–1284.
- (34) Toby, B. H.; Von Dreele, R. B. GSAS-II: the genesis of a modern open-source all purpose crystallography software package. *Journal of Applied Crystallography* **2013**, *46*, 544–549.
- (35) Angel, R. J.; Alvaro, M.; Gonzalez-Platas, J. EosFit7c and a Fortran module (library) for equation of state calculations. *Z. Kristallogr. Cryst. Mater.* **2014**, *229*, 405–419.
- (36) Birch, F. Finite elastic strain of cubic crystals. *Physical review* **1947**, *71*, 809.
- (37) Murnaghan, F. D. The compressibility of media under extreme pressures. *Proceedings of the National Academy of Sciences* **1944**, *30*, 244–247.
- (38) Deller, K.; Eisenmann, B. Ternäre Erdalkali-Element (V)-Verbindungen  $AMg_2B_2$  mit  $A = Ca, Sr, Ba$  und  $B = As, Sb, Bi$ /Ternary Alkaline Earth-Element (V)-Compounds  $AMg_2B_2$  with  $A = Ca, Sr, Ba$  and  $B = As, Sb, Bi$ . *Zeitschrift für Naturforschung B* **1977**, *32*, 612–616.
- (39) May, A. F.; McGuire, M. A.; Singh, D. J.; Custelcean, R.; Jellison Jr, G. E. Structure and properties of single crystalline  $CaMg_2Bi_2$ ,  $EuMg_2Bi_2$ , and  $YbMg_2Bi_2$ . *Inorganic chemistry* **2011**, *50*, 11127–11133.
- (40) Poirier, J.-P.; Tarantola, A. A logarithmic equation of state. *Physics of the Earth and Planetary Interiors* **1998**, *109*, 1–8.
- (41) Shannon, R. D. Revised effective ionic radii and systematic studies of interatomic distances in halides and chalcogenides. *Acta crystallographica section A: crystal physics, diffraction, theoretical and general crystallography* **1976**, *32*, 751–767.
- (42) Angel, R. J. Equations of state. *Reviews in mineralogy and geochemistry* **2000**, *41*, 35–59.
- (43) Hazen, R. M.; Finger, L. W. Bulk modulus—volume relationship for cation-anion polyhedra. *Journal of Geophysical Research: Solid Earth* **1979**, *84*, 6723–6728.
- (44) Cohen, M. L. Calculation of bulk moduli of diamond and zinc-blende solids. *Physical Review B* **1985**, *32*, 7988.

# Supplementary Information

## S1 Selected crystallographic data for the ambient- and high-pressure phases

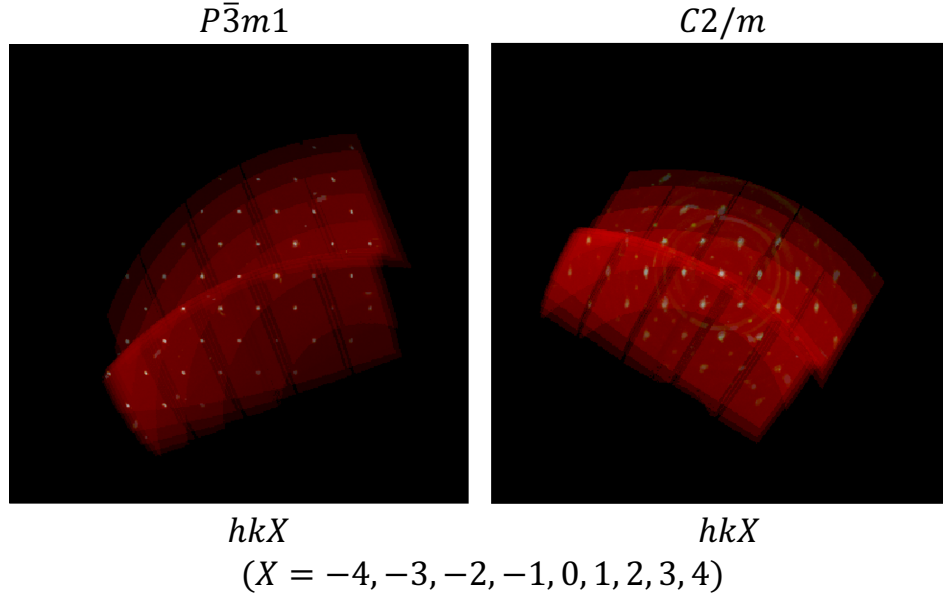


Figure S1: Precession images for  $\text{YbMg}_2\text{Bi}_2$  at pressures below (left) and above (right) the transition. The crystal quality below the transition pressure is excellent, while significant broadening of reflections is observed above the transition pressure. However, there is clear evidence of decreased symmetry, consistent with the powder diffraction patterns.

Table S1: Crystallographic data for the trigonal  $\text{CaMg}_2\text{Bi}_2$  structure at different pressures from single crystal XRD experiments.

Pressure (GPa)	AP	3.0	4.9	7.4	10.2
Space Group; Z	$P\bar{3}m1$ ; 1	$P\bar{3}m1$ ; 1	$P\bar{3}m1$ ; 1	$P\bar{3}m1$ ; 1	$P\bar{3}m1$ ; 1
a (Å)	4.71886(17)	4.6483(19)	4.6223(15)	4.549(2)	4.472(2)
b (Å)	4.71886(17)	4.6483(19)	4.6223(15)	4.549(2)	4.472(2)
c (Å)	7.6412(3)	7.486(4)	7.431(3)	7.283(4)	7.135(4)
Volume (Å <sup>3</sup> )	147.356(10)	140.09(11)	137.49(8)	130.54(10)	123.57(11)
Meas. Reflections; $R_{\text{int}}$	313; 12.98	109; 5.78	121; 5.96	144; 7.76	131; 5.18
No. of indep. reflections	28	56	71	119	80
$R_1$ ; $wR_2$ (all intensities)	10.88; 23.57	12.29; 33.32	17.38; 44.00	12.59; 30.12	14.99; 48.20
GoF	1.4147	1.8207	1.4868	1.5871	2.7204

## S2 Volume calculation of polyhedra and error estimations

The volumes of the octahedra and tetrahedra were calculated by treating them as regular polyhedra, using an average of the two distinct Bi-Bi bond distances as the edge length of the octahedron ( $l_{\text{oct}}$ ) and of the tetrahedron ( $l_{\text{tet}}$ ). The octahedron ( $V_{\text{oct}}$ ) and tetrahedron ( $V_{\text{tet}}$ ) volumes are then calculated as:

$$V_{\text{oct}} = \frac{\sqrt{2}l_{\text{oct}}^3}{3} \quad (\text{S1})$$

Table S2: Crystallographic data for the trigonal  $\text{YbMg}_2\text{Bi}_2$  structure at different pressures from single crystal XRD experiments.

Pressure (GPa)	AP	3.4	5.2	7.1	10.0
Space Group; Z	$P\bar{3}m1$ ; 1	$P\bar{3}m1$ ; 1	$P\bar{3}m1$ ; 1	$P\bar{3}m1$ ; 1	$P\bar{3}m1$ ; 1
a (Å)	4.7149(4)	4.6502(11)	4.6034(4)	4.5624(6)	4.5058(8)
b (Å)	4.7149(4)	4.6502(11)	4.6034(4)	4.5624(6)	4.5058(8)
c (Å)	7.6063(7)	7.474(3)	7.3782(7)	7.2937(10)	7.1702(13)
Volume (Å <sup>3</sup> )	146.43(2)	139.98(7)	135.406(19)	131.48(3)	126.07(4)
Meas. Reflections; R <sub>int</sub>	152; 6.66	65; 2.42	126; 3.18	123; 2.80	126; 3.08
No. of indep. reflections	1096	161	347	324	315
R <sub>1</sub> ; wR <sub>2</sub> (all intensities)	2.99; 7.05	3.83; 11.58	4.94; 27.52	5.71; 18.17	7.09; 20.31
GoF	1.106	1.369	1.422	1.228	1.286

Table S3: Crystallographic data for the monoclinic phase of  $\text{CaMg}_2\text{Bi}_2$  and  $\text{YbMg}_2\text{Bi}_2$ .

	$\text{CaMg}_2\text{Bi}_2$	$\text{YbMg}_2\text{Bi}_2$
Pressure (GPa)	12.8	11.6
Space Group; Z	$C2/m$ ; 2	$C2/m$ ; 2
a (Å)	7.65(3)	7.558(7)
b (Å)	4.333(3)	4.489(6)
c (Å)	7.082(10)	7.081(6)
$\beta$ (°)	94.36(4)	91.82(7)
Volume (Å <sup>3</sup> )	234.2(9)	240.1(4)
Meas. Reflections; R <sub>int</sub>	70; 1.54	128; 3.90
No. of indep. Reflections	69	290
R <sub>1</sub> ; wR <sub>2</sub> (all intensities)	9.60; 26.20	18.31; 50.16
GoF	1.525	2.043

Table S4: Structure parameters of the high-pressure structure for  $\text{CaMg}_2\text{Bi}_2$  at 12.8 GPa. Note that the uncertainty for the Mg atom is significantly higher than those observed for Ca and Bi. These elevated values strongly suggests significant disorder or positional uncertainty for the Mg atom.

Atom	x	y	z	Occ.	$U_{eq}$ (Å <sup>2</sup> )	Site	Sym.
Ca	1.000(3)	1.000(3)	0.000(1)	1.000	0.020	2a	2/m
Bi	0.648(2)	1.000(3)	0.253(1)	1.000	0.028	4i	m
Mg	0.850(17)	0.500(30)	0.385(11)	1.000	0.030	4i	m

Table S5: Structure parameters of the high-pressure structure for  $\text{YbMg}_2\text{Bi}_2$  at 11.6 GPa

Atom	x	y	z	Occ.	$U_{eq}$ (Å <sup>2</sup> )	Site	Sym.
Yb	0.500(1)	0.500(1)	1.000(1)	1.000	0.050	2a	2/m
Mg	0.161(6)	0.500(1)	0.647(4)	1.000	0.037	4i	m
Bi	0.172(1)	0.500(1)	0.239(1)	1.000	0.050	4i	m

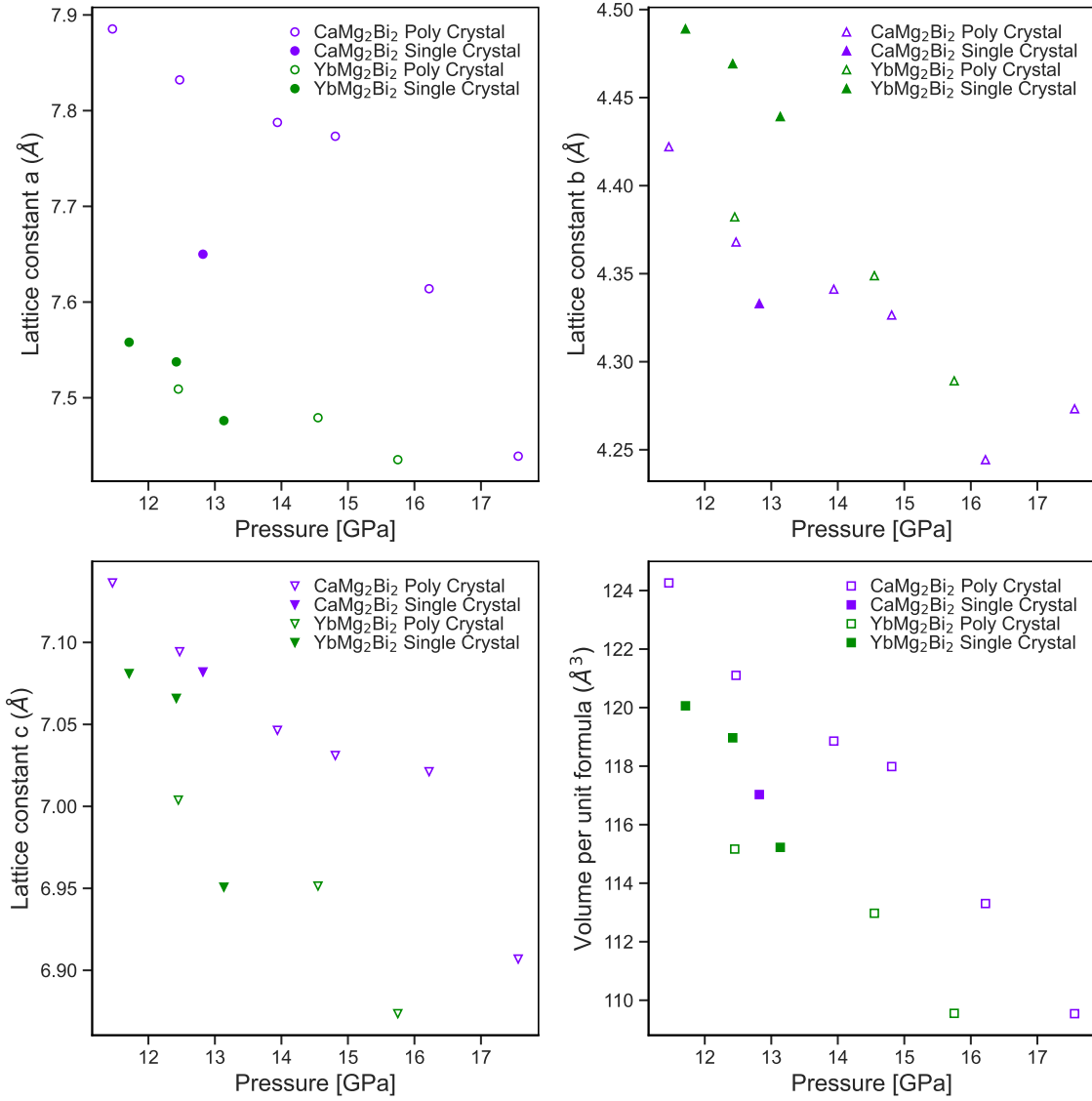


Figure S2: Lattice parameters for the  $C2/m$  structure above the phase transition for the single- and poly-crystal available data. Note that the volume per unit formula is shown.

and

$$V_{tet} = \frac{l_{tet}^3}{6\sqrt{2}} \quad (S2)$$

respectively. To calculate the uncertainty in the polyhedral volume, an error propagation scheme was calculated that starts with the uncertainty in the bond lengths as is explained next. For the octahedron volume, the longer Bi-Bi bond length ( $l_{octI}$ ) and the corresponding uncertainty of such bond ( $u_{octI}$ ) was used to determine the maximum octahedral volume  $V_{oct,max}$  as:

$$V_{oct,max} = \frac{\sqrt{2}(l_{octI} + u_{octI})^3}{3} \quad (S3)$$

Similarly, the minimum octahedron volume  $V_{oct,min}$  is calculated using the shorter Bi-Bi bond length ( $l_{octII}$ ) and its associated uncertainty ( $u_{octII}$ ):

$$V_{oct,min} = \frac{\sqrt{2}(l_{octII} - u_{octII})^3}{3} \quad (S4)$$

Likewise, the maximum tetrahedron volume ( $V_{tet,max}$ ) is calculated as a regular polyhedron via the longer Bi-Bi bond ( $l_{tetI}$ ) and its uncertainty ( $u_{tetI}$ ), as a modification of equation S1. It becomes:

$$V_{tet,max} = \frac{(l_{tetI} - u_{tetI})^3}{6\sqrt{2}} \quad (S5)$$

Conversely, the minimum tetrahedron volume ( $V_{tet,min}$ ) is based on the smaller Bi-Bi bond that spans the polyhedron ( $l_{tetII} = l_{octI}$ ) and its corresponding uncertainty ( $u_{tetII} = u_{octI}$ ), which is then:

$$V_{tet,min} = \frac{(l_{tetII} - u_{tetII})^3}{6\sqrt{2}} = \frac{(l_{octI} - u_{octI})^3}{6\sqrt{2}} \quad (S6)$$

which, again, is a modification of equation S2.

Now, in order to calculate the total polyhedral volume error ( $e_{Vol}$ ), the *symmetric* mean absolute percentage error is obtained with the following general relation:

$$e_V = \frac{1}{n} \sum_{i=1}^n \left| \frac{V_{avg} - V_i}{2(V_{avg} + V_i)} \right| \quad (S7)$$

where  $V_{avg}$  is the average volume and  $V_i$  the extreme volumes, i.e., either  $V_{max}$  or  $V_{min}$ . Then, using equation S7 the octahedral ( $e_{V_{oct}}$ ) and tetrahedral volume ( $e_{V_{tet}}$ ) errors become:

$$e_{V_{oct}} = \frac{1}{2} \left[ \left| \frac{V_{oct} - V_{oct,max}}{2(V_{oct} + V_{oct,max})} \right| + \left| \frac{V_{oct} - V_{oct,min}}{2(V_{oct} + V_{oct,min})} \right| \right] \quad (S8)$$

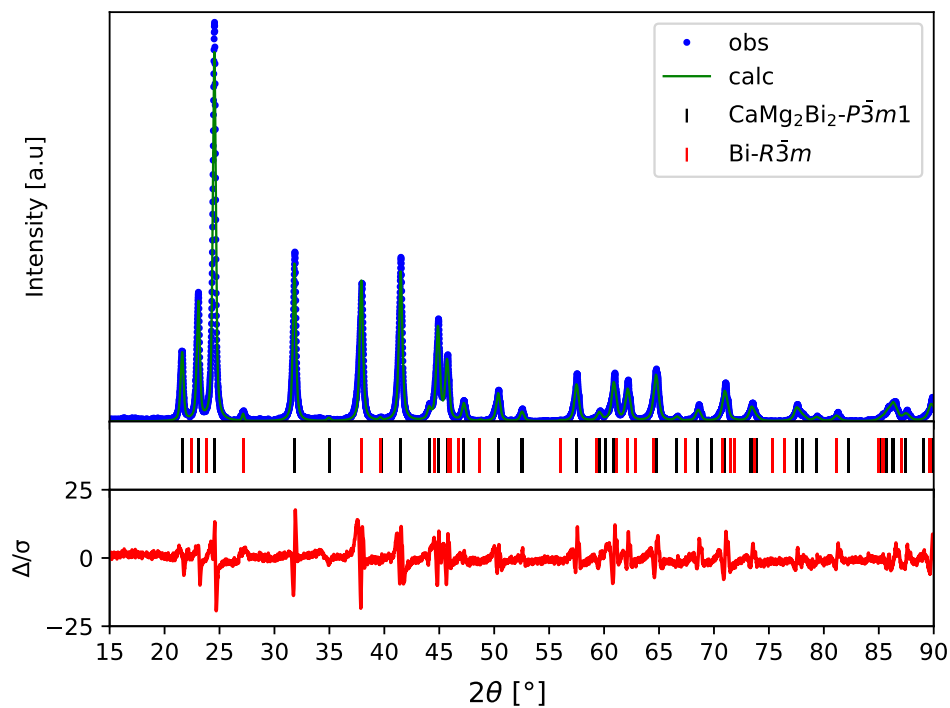
and

$$e_{V_{tet}} = \frac{1}{2} \left[ \left| \frac{V_{tet} - V_{tet,max}}{2(V_{tet} + V_{tet,max})} \right| + \left| \frac{V_{tet} - V_{tet,min}}{2(V_{tet} + V_{tet,min})} \right| \right] \quad (S9)$$

respectively.

### S3 Rietveld refinements

(a)



(b)

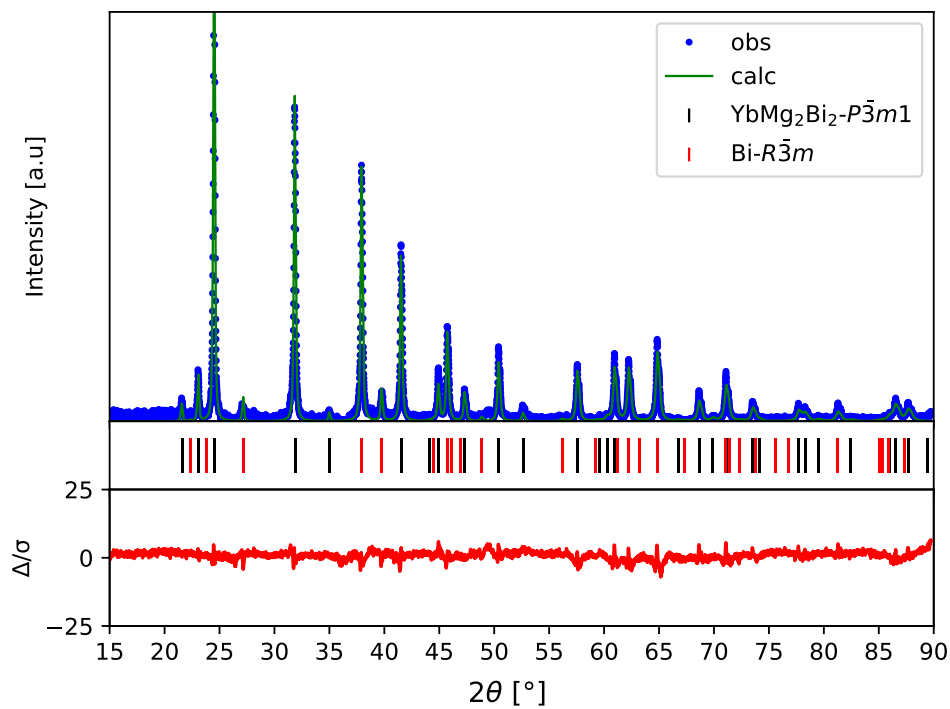
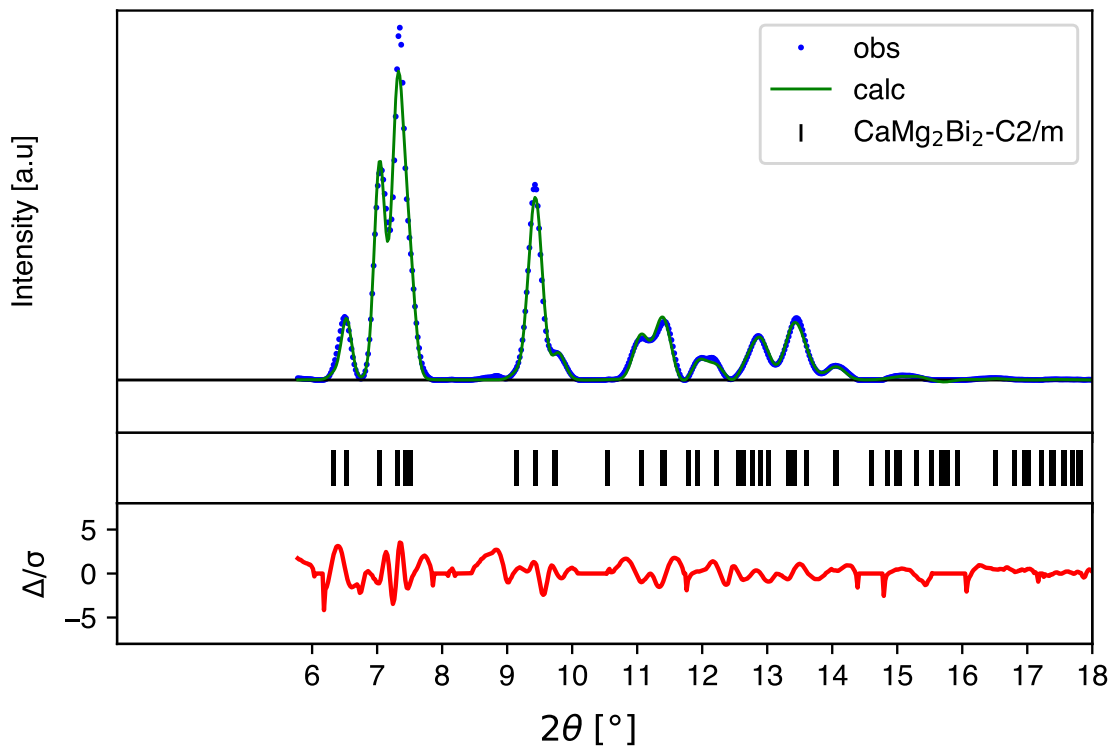


Figure S3: Ambient-pressure ( $P\bar{3}m1$ ) Rietveld refinements of a)  $\text{CaMg}_2\text{Bi}_2$  and b)  $\text{YbMg}_2\text{Bi}_2$ . In a), the Bi impurity phase is around 3%. In b), the content of Bi is approx. 5%.

(a)



(b)

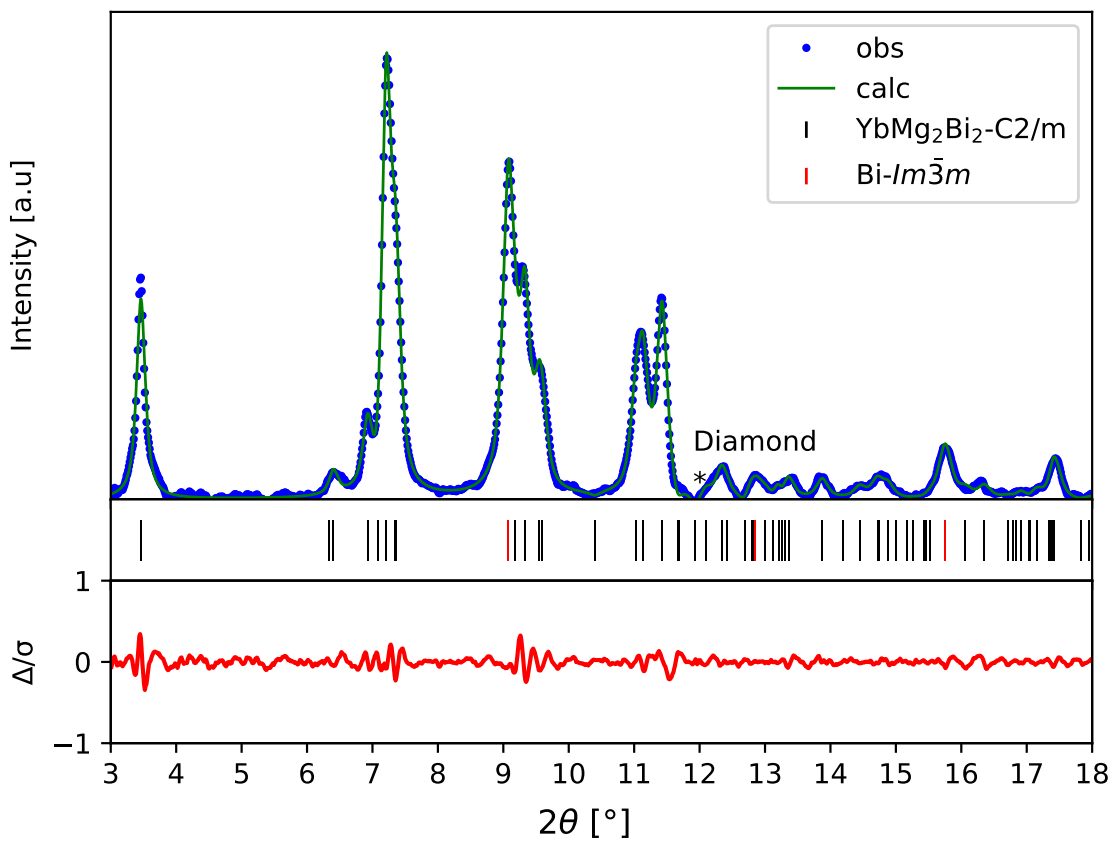


Figure S4: High-pressure (*C2/m*) Rietveld refinements for a) CaMg<sub>2</sub>Bi<sub>2</sub> at 12.47 GPa and b) YbMg<sub>2</sub>Bi<sub>2</sub> at 12.45 GPa.